The polymorphic behaviour of Wigner bilayers
Supplementary material

Moritz Antlanger, Gerhard Kahl, Martial Mazars, Ladislav Šamaj, and Emmanuel Trizac
(Dated: July 11, 2016)

We present here the numerical techniques employed (of evolutionary and Monte Carlo type), together with the analytical framework for exact energy calculations.

I. NUMERICAL TECHNIQUES

A. Computation of the total energy with the Ewald method

For the asymmetric bilayers, the distribution of the electric point charges (with nominal value $-e$) and of the uniform neutralising background on layers 1 and 2 [$e\sigma_1(\boldsymbol{r})$ at $z=0$ and $e\sigma_2(\boldsymbol{r})$ at $z=d$] is given by

$$\rho(\boldsymbol{r}) = -e\sum_{i\in L_1}\delta(\boldsymbol{r}_i-\boldsymbol{r})\delta(z_i) - e\sum_{i\in L_2}\delta(\boldsymbol{r}_i-\boldsymbol{r})\delta(z_i-d) + e\sigma_1(\boldsymbol{r})\delta(z) + e\sigma_2(\boldsymbol{r})\delta(z-d), \tag{1}$$

δ being the Dirac distribution. The two parallel plates are of infinite extent. The inter-plate space $0\le z\le d$ and the whole system is electro-neutral. It is filled with a solution of fixed dielectric constant, equal to that of the walls, so that no image charges ensue.

The total energy of the system can be computed as a sum of Coulomb interactions via

$$\begin{aligned} E = {} & \frac{e^2}{2}\sum_{i\in L_1\bigcup L_2}\sum_{j\in L_1\bigcup L_2}{\sum_{\boldsymbol{S_n}}}'\frac{1}{\mid \boldsymbol{r}_{ij}+\boldsymbol{S_n}\mid} - \frac{e^2}{2}\sum_{i\in L_1\bigcup L_2}\int_{L_1\bigcup L_2}d\boldsymbol{r}\sum_{\boldsymbol{S_n}}\frac{\rho(\boldsymbol{r})}{\mid \boldsymbol{r}_i-\boldsymbol{r}+\boldsymbol{S_n}\mid} \\ & + \frac{e^2}{2}\int_{L_1\bigcup L_2}d\boldsymbol{r}'\int_{L_1\bigcup L_2}d\boldsymbol{r}\sum_{\boldsymbol{S_n}}\frac{\rho(\boldsymbol{r})\rho(\boldsymbol{r}')}{\mid \boldsymbol{r}-\boldsymbol{r}'+\boldsymbol{S_n}\mid}. \end{aligned} \tag{2}$$

The $\mathbf{r}_i$ and $\mathbf{r}_j$ are the particle positions with $\mathbf{r}_{ij}=\mathbf{r}_i-\mathbf{r}_j$; L_1 and L_2 denote the two layers. Further, $\boldsymbol{S}_0$ denotes the simulation box (with the primitive vectors $\boldsymbol{a}$ and $\boldsymbol{b}$) and the periodic images of $\boldsymbol{S}_0$ are defined by $\boldsymbol{S_n}=n_a\boldsymbol{a}+n_b\boldsymbol{b}$ with $(n_a,n_b)\in\mathbb{Z}^2$ (the simulation cell is replicated perpendicular to the z-direction); the prime in the above summation indicates that contributions with $i=j$ are excluded from the summations in $\boldsymbol{S}_0$.

We now split the total energy into intra-layer (index a) and inter-layer (index e) contributions as

$$E = E_1^{(a)} + E_2^{(a)} + E_{12}^{(e)}. \tag{3}$$

With the Ewald method, we obtain [1] for the *intra-layer* energy for layer $\ell=(1,2)$

$$E_\ell^{(a)} = \frac{e^2}{2}\sum_{i,j\in L_\ell}{\sum_{\boldsymbol{S_n}}}'\frac{\mathrm{erfc}(\alpha\mid \boldsymbol{s}_{ij}+\boldsymbol{S_n}\mid)}{\mid \boldsymbol{s}_{ij}+\boldsymbol{S_n}\mid} + \frac{\pi e^2}{S}\sum_{\boldsymbol{G}\neq 0}\frac{\mathrm{erfc}(G/2\alpha)}{G}\left|\sum_{i\in L_\ell}\exp\left(j\boldsymbol{G}.\boldsymbol{s}_i\right)\right|^2 - \frac{\sqrt{\pi}N_\ell^2e^2}{\alpha S} - \frac{\alpha N_\ell e^2}{\sqrt{\pi}}; \tag{4}$$

here N_ℓ is the number of point charges in layer ℓ, S is the area of $\boldsymbol{S}_0$, α stands for the Ewald damping parameter and the $\boldsymbol{G}$ are the wave vectors in reciprocal space [1]. Finally, the *inter-layer* energy is given by

$$\begin{aligned} E_{12}^{(e)} = {} & e^2\sum_{i\in L_1}\sum_{i\in L_2}{\sum_{\boldsymbol{S_n}}}'\frac{\mathrm{erfc}\left(\alpha\sqrt{\mid \boldsymbol{s}_{ij}+\boldsymbol{S_n}\mid^2+d^2}\right)}{\sqrt{\mid \boldsymbol{s}_{ij}+\boldsymbol{S_n}\mid^2+d^2}} + \frac{\pi e^2}{S}\sum_{\boldsymbol{G}\neq 0}\mathrm{F}(G,\alpha;d)\,\mathcal{R}\left[\left(\sum_{i\in L_1}e^{i\boldsymbol{G}\cdot\boldsymbol{s}_i}\right)\left(\sum_{i\in L_2}e^{-i\boldsymbol{G}\cdot\boldsymbol{s}_i}\right)\right] \\ & - \frac{\pi N_1N_2e^2}{S}\left[\frac{e^{-\alpha^2d^2}}{\alpha\sqrt{\pi}} + d\,\mathrm{erf}(\alpha d)\right] - \pi e^2\sigma_2 d\left[\sigma_1 S - 2N_1\right] - \pi e^2\sigma_1 d\left[\sigma_2 S - 2N_2\right], \end{aligned} \tag{5}$$

introducing

$$\mathrm{F}(G,\alpha;d) = \frac{1}{G}\left[\exp(Gd)\,\mathrm{erfc}\left(\frac{G}{2\alpha}+\alpha d\right) + \exp(-Gd)\,\mathrm{erfc}\left(\frac{G}{2\alpha}-\alpha d\right)\right] \tag{6}$$

d being the distance between the layers and $G=|\mathbf{G}|$.

B. Bond-orientational order parameters and classification of structures

The bond-orientational order parameters (BOOPs) [2] have been computed for each layer in a similar way as in Ref. [3]. Here, the neighbours of a tagged particle are identified with a Voronoi construction [4]; the number of nearest neighbours of particle i is denoted by N_i.

For a given configuration, the BOOPs are defined by

$$\Psi_n^{(L)} = \frac{1}{N_L}\Big|\sum_{i\in L}\frac{1}{\sum_{j\in\mathcal{N}_i} l_{ij}}\sum_{j\in\mathcal{N}_i} l_{ij}\exp(\imath\, n\,\theta_{ij})]\Big| \tag{7}$$

where $j \in \mathcal{N}_i$ denotes that particle j is a nearest neighbour of particle i; l_{ij} is the length of the Voronoi polygon shared by particles i and j [5], θ_{ij} is the angle between the projection of the inter-particle vector $\mathbf{r}_{ij}$ onto one of the planes and an arbitrary, fixed direction, and n is an integer. In Eq. (7), the superscript index (L) refers to the four different methods of Voronoi construction used for calculating the BOOPs : for layer 1 (index 1), for layer 2 (index 2), or for all particles after projecting them onto the same plane (index 3). In addition, we also calculate modified BOOPs (index 4) to quantify the geometry of "holes", i.e., of particles in layer 2 and the surrounding particles in layer 1. We have computed BOOPs for $n = 4, 5, 6, 7, 8, 10, 12, 18$ and 24. In the Evolutionary Algorithm route, the order parameters are computed only for the configuration that corresponds to the global energy minimum for a given state point. On the other hand, the order parameters are averaged along the simulation runs in the Monte Carlo approach.

We classify ordered structures first by the value of x and then further refine using one or more BOOPs; the relevant criteria for identifying structures are listed in Table I. Note that the cutoff values for the BOOPs (third column) are to some extent arbitrary.

TABLE I: Criteria for identifying the various structures, from the values of the bond orientational order parameters (BOOPs).

I	$x = 0$		hexagonal monolayer
II	$x = 1/2$	$\Psi_4^{(1,2)} = 1$, $0 < \Psi_6^{(1,2)} < 1$	rectangular bilayer
III	$x = 1/2$	$\Psi_4^{(1,2)} = 1$, $\Psi_6^{(1,2)} = 0$	square bilayer
IV	$x = 1/2$	$0 < \Psi_4^{(1,2)} < 1$, $0 < \Psi_6^{(1,2)} < 1$	rhombic bilayer
V	$x = 1/2$	$\Psi_4^{(1,2)} = 0$, $\Psi_6^{(1,2)} = 1$	hexagonal bilayer
I_x	$0 < x < 1/3$	$\Psi_6^{(3)} > 0.9$	
H	$x = 1/3$	$\Psi_6^{(3)} > 0.9$	honeycomb (layer 2)
II_x	$1/3 < x < 1/2$	$\Psi_6^{(3)} > 0.9$	
V_x	$0 < x < x_{\rm neutr}$	$(1-x)\Psi_6^{(1)} + x\Psi_6^{(2)} > 0.9$	hexagonal bilayer
DV_x	$2/5 \le x < 1/2$	$0.5 \le \Psi_6^{(1,2)}$, $\Psi_4^{(1)} \sim 0.4$, $\Psi_5^{(2)} \sim 0.3$	Distorted hexagons
S_1	$x = 1/3$	$\Psi_5^{(1)} > 0.9$, $\Psi_4^{(2)} > 0.9$	snub square (layer 1)
Pentagonal structures			
S_2	$x = 1/3$	$\Psi_5^{(2)} > 0.45$	snub square (layer 2)
P-type	$1/3 < x < 1/2$	$\Psi_5^{(2)} > 0.45$	pentagonal in layer 2
	or $0 < x < 1/3$	or $\Psi_5^{(4)} > 0.9$	pentagonal holes

C. Computations based on Evolutionary Algorithms (EAs)

In our effort to identify ground state configurations, we use an optimisation tool based on ideas of Evolutionary Algorithms (EAs) [6]. EAs are heuristic approaches to search for global minima in high-dimensional search spaces that are characterised by rugged energy landscapes.

We introduce a unit cell which creates (together with its periodic images) a system of infinite extent. The periodic boundary conditions are in compliance with the Ewald summation technique. Inside this cell, the particles are located in such a way as to minimise the internal energy of the system. We initialise the algorithm by creating a set of random particle arrangements. These configurations are graded by their fitness value, a quantity that provides evidence on how suitable this configuration is to solve the optimisation problem. Since we are interested in finding ground state structures, a high fitness value of a particular configuration corresponds to a low value of the energy per particle.

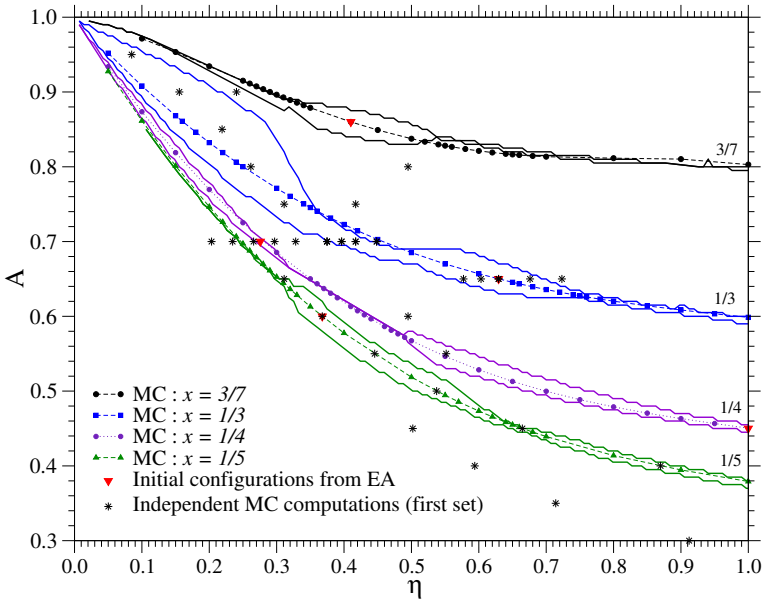

FIG. 1: The symbols indicate the state points for which Monte Carlo simulations have been performed. The continuous curves delineate regions in the phase diagram with a constant value of order parameter $x = N_2/N$ (as labeled) initially found with EA computations. The dashed lines are particular paths, inside or close to the constant x regions, where a particular Monte Carlo effort has been invested (see main text).

We then iteratively use existing configurations to create new ones by applying one of two operations: crossover and mutation. In the former one, we first select two configurations where the choice is biased by high fitness values. Traits of both particle arrangements (such as lattice vectors and/or particle positions) are then combined to form a new configuration. The mutation operation, on the other hand, introduces random changes to a randomly chosen configuration, such as moving an arbitrarily chosen particle or distorting the lattice vectors. Typically 2000 iterations are required for a particular state point until proper convergence towards the global minimum has been achieved.

Our implementation of EAs is memetic, i.e., we combine global and local search techniques: every time a new configuration has been created with one of the two above mentioned EA operations, we apply the L-BFGS-B [7] algorithm which guides us to the nearest local minimum.

We consider unit cells with sizes ranging between one and 40 particles, the latter value being imposed by computational limitations. To find the optimised particle configuration we proceed as follows: (i) we do not allow particles to move from one layer to the other and consider all possible values of $x \leq 0.5$ that are compatible with the number of particles per cell; according to our experience, this strategy improves the convergence speed when sampling the search space. (ii) We then fix $A = 0$ and perform computations for 201 evenly-spaced values of $\eta \in [0, \sqrt{2}]$. We thus obtain the optimised energy-values $E(\eta, x, A = 0)$. (iii) We then proceed to $A > 0$ and vary this quantity on a grid of 201 evenly-spaced values of $A \in [0, 1]$. The optimised energy for these configurations $E(\eta, x, A)$ is then obtained by exploiting the A-dependence of the last two terms in Eq. (5) via

$$E(\eta, x, A) = E(\eta, x, A = 0) + 2^{3/2}\pi\eta N\sqrt{\sigma_1 + \sigma_2}e^2\frac{A}{(1+A)^2}(A - 2x - 2xA), \tag{8}$$

see also Eq. (17) below. For a given state point (η, A) we retain only the configuration with the lowest energy per particle E/N as the ground state.

For a closer investigation of certain transitions between minima, we employ a related Energy Minimisation (EM) approach: here we construct starting configurations suggested by the analytical approach and then locally optimise the particle positions using the L-BFGS-B algorithm [7]. This strategy allows us to study specific problems on a finer grid in phase space and to increase, concomitantly, the unit cell size to up to 101 particles.

D. Monte Carlo (MC) simulations

To provide an estimate for the stability of the ordered structures predicted by the EA investigations, we have performed Monte Carlo (MC) simulations at finite but small temperature T for considerably larger systems (typically $N \simeq 4000$). MC simulations are carried out in the canonical ensemble assuming a variable shape of the simulation box $\boldsymbol{S}_0$, but with a fixed surface area S. Trial moves for the shape of the box in combination with the Ewald method are documented in Ref. [8]; this method is particularly well adapted to study solid-solid and solid-liquid transitions

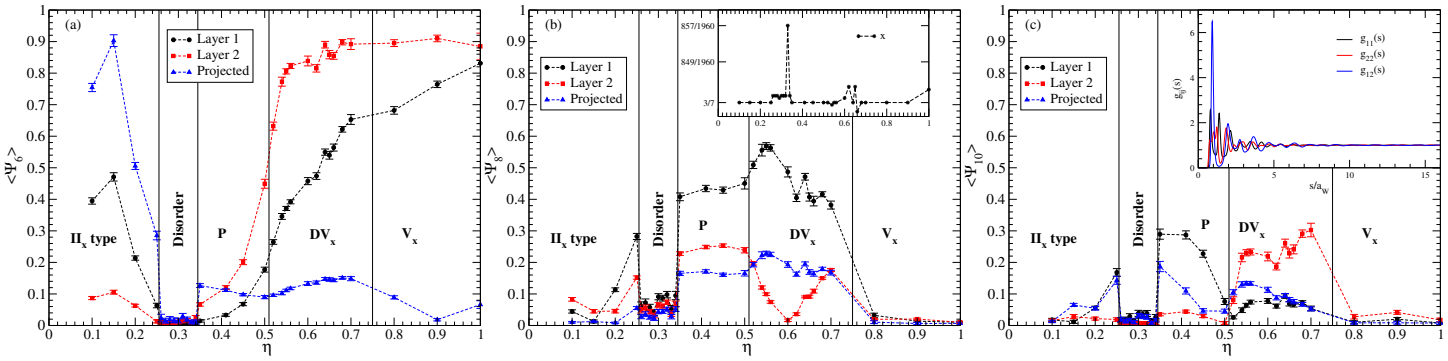

FIG. 2: Average bond orientational order parameters computed with Monte Carlo simulations for runs with $x = 3/7$: (a) $\langle\Psi_6\rangle$, (b) $\langle\Psi_8\rangle$ [inset : value of $x = N_2/N$ obtained in MC simulations] and (c) $\langle\Psi_{10}\rangle$ [Inset : center-to-center correlations functions computed in Monte Carlo simulations in the disordered region - $\eta = 0.27$ and $A = 0.908$]. The label of the crystal phases identified in MC are reported on the figures and the value of A for a given η is given by $A(\eta) = 1 - 0.2132\eta - 0.8947\eta^2 + 1.773\eta^3 - 0.8562\eta^4$ (this curve is vizualized in Fig. 1 as a dashed line).

and has been successfully applied for the study of the crystal phases of Coulomb [8], Yukawa bilayers [3], and Wigner monolayer [10].

For $\eta = 0$, our system is equivalent to a one component plasma confined to a plane (OCP-2D); the ground state is then a triangular lattice (i.e., our structure I). The only relevant thermodynamical variable that characterises the OCP-2D system is the coupling constant Γ, defined via $\Gamma = e^2\sqrt{\pi(\sigma_1+\sigma_2)}/k_BT$. Melting of structure I in the OCP-2D system occurs at $\Gamma \simeq 140$ [10]. In an effort to remain very close to the ground state of the bilayer, we have chosen the temperature in all MC simulations of the present study such that $1500 \leq \Gamma \leq 2000$.

We define a MC-cycle as N trial moves of randomly chosen particles and a trial change of the shape of the simulation box. The trial moves of the particles are realised as translations within the layer the particle belongs to (in 90-97 percent of the cases) or a trial move of this particle from one layer to the other one (in 3-10 percent of the cases). Equilibration is realised during $0.3-1.6\times10^6$ MC-cycles; subsequently ensemble averages are taken over $0.3-1.0\times10^6$ MC-cycles; numerical Voronoi constructions [4] are performed after each MC-cycle.

The 170 state points in the (η, A)-plane for which intensive MC simulations have been carried out are specified in Fig. 1. Two sets of simulations have been performed:

(i) The first set (represented by the isolated stars in Fig. 1) use as initial configurations particle arrangements that have been identified in preceding EA runs. However, since the number of particles in the primitive cell of the predicted structures differ from one state point to the other, it is difficult to observe a transition between two ordered structures in an MC simulation at some fixed N.

(ii) To overcome this difficulty, we have performed a second set of MC computations for which the ordered structures are throughout compatible with the number of particles used (see also Fig. 3). The state points for this second set of MC simulations are marked in Fig. 1 by dots that are connected by the dotted lines; they are defined such that the value of $x = N_2/N$ varies only slightly along these lines (according to the results obtained by the EA approach). The curves $A = A(\eta)$ indicated in Fig. 1 are parameterised as simple polynomials in η. MC simulations of all state points pertaining to one of these curves are launched from one particular EA-based particle configuration. For MC in the second set, the initial configuration is chosen from a configuration obtained with EA computations ; for each curve, the initial configuration is represented by a red triangle in Fig. 1. The distance η is then gradually changed, and the ground state found at a given state-point is used as the next initial condition of the iteration. In doing so, one moves along the lines displayed, and the very same transitions are obtained as those predicted by EA, without any hysteresis (as shown by the variations of the order parameters in Fig. 2).

The first set of MC simulations allows us to estimate the stability of the ordered structures predicted in the EA approach at finite temperature and for considerably larger systems. In contrast, the second set of simulations provides the possibility to observe transitions between commensurable ordered structures. Throughout, the structures of phases obtained with the MC and EA approaches were found to be in very good agreement.

The MC simulations in the second set of computations with $x = 3/7$ are useful to outline some effects of the thermal fluctuations on the stability of the crystal phases found in EA computations. On Fig.2, we report the average bond orientational order parameters Ψ_6, Ψ_8 and Ψ_{10} computed in MC with (η, A) constrained on the line $x = 3/7$ in

Fig.1. In the inset of Fig.2 (b), we show the variations of x computed with MC simulations. For all the computations reported here, the initial configuration is the pentagonal P phase found in EA with $\eta = 0.41$ and $A = 0.86$. The variations of the BOOPs allow us to identify unambiguously four crystal phases: II_x, P, V_x, in full agreement with EA computations. The phase named Distorted-V_x (DV_x), also present at EA level, is identified with a quite large value of the order parameter Ψ_8 (~ 0.45) for Layer 1 and a significant value of Ψ_{10} (~ 0.3) for Layer 2.

In Fig.3, we show the structure of the phase DV_x with Voronoi constructions computed in EA (panels a and b) and obtained in MC simulations (panel c). The Voronoi constructions for phases V_x in both layers realize monohedral tilings with regular hexagons ; in both layers the symmetry group of the tiling is the group **p6m** (wallpaper group). As shown on Fig.3 (a,b), the Voronoi constructions for both layers of phases DV_x are tilings with distorted hexagons. The tiling for Layer 1 is dihedral, Fig.3 (a) and, for Layer 2, the tiling is monohedral and its symmetry group is **cmm**, Fig.3 (b) [9]. The identification of the DV_x phases in EA is difficult since the number of particles per primitive cell is not constant, it ranges from 10 to 40. In these phases, the value of x is not constant too. Phases DV_x were identified in EA after MC simulations and results shown on Fig.2 and a systematic examination of the snapshots as the one shown in 3(c).

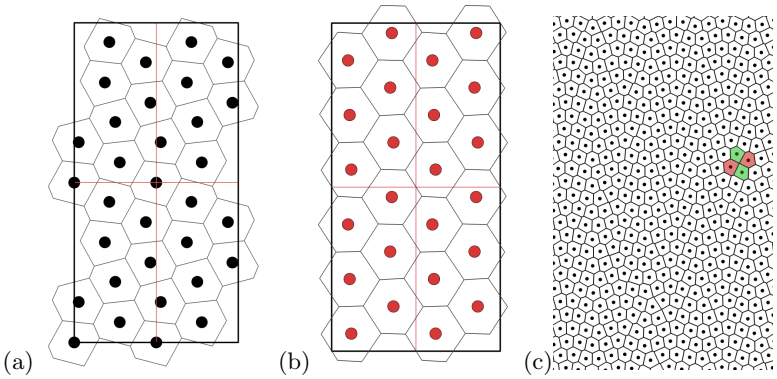

FIG. 3: Structure of the phase DV_x with Voronoi constructions. (a,b) Configurations predicted by EA computations for $A = 0.82$ and $\eta = 0.7$: (a) the Voronoi constructions are done by including in the computation only the particles in Layer 1 (in black) and (b) same for Layer 2, the particles are represented in red ; nine primitive cells are represented. (c) Layer 1 of the DV_x phase ($\eta = 0.7$, $A = 0.814$) obtained in MC simulations. The Voronoi cells represented in green have 5 sides, in white 6 sides and in red 7 sides.

It is worthwhile to mention that in MC computations reported in Fig. 2, long range order is absent for $0.255 \leq \eta \leq 0.345$; in this window, the order parameters in Fig. 2 vanish; this can also be appreciated on the variations of the intra and inter-layer correlation functions shown in the inset of Fig. 2 (c). We interpret this lack of order, in spite of the smallness of temperature, as resulting from a strong competition between the neighboring phases (see the general phase diagram in the main text, indicating that the region under scrutiny here is where the domains of prevalence of structures II_x, H, III and P are very close). The abrupt variations of the order parameters close to the boundaries of this disordered region are indications of first order transitions and coexistences between the various phases.

Before closing this subsection, we add that the results of MC computations (not shown) performed with $x = 1/3$, $1/4$ and $1/5$ (cf. Fig.1) agree as well with EA computations as the results for $x = 3/7$.

II. "LARGE" VALUES OF A, TRANSITION BETWEEN PHASES I AND I_x

A. Stability of structure I at small distances

When the two plates are at contact ($\eta = 0$), the lowest energy of the particle system corresponds to the hexagonal Wigner lattice (phase I, see the main document), with lattice spacing ruled by electro-neutrality

$$\frac{\sqrt{3}}{2} a^2 (\sigma_1 + \sigma_2) = 1. \tag{9}$$

Let us increase η to a non-zero value and suppose that all particles forming the hexagonal Wigner structure will stay on plate 1; such a phase will be coined as I, too. Whether or not phase I is favourable for particles can be

tested qualitatively by taking one of the particles perpendicularly from plate 1 at $z = 0$ to plate 2 at $z = d$. This is accompanied by the increase of particle's potential energy by $\Delta E_{\rm pot} = 2\pi e^2(\sigma_1 - \sigma_2)d$. Simultaneously, since the distance of the reference particle to all other particles increases, its interaction energy decreases by $\Delta E_{\rm int} \sim -e^2 s d^2$ (s is a structure constant of the hexagonal Wigner lattice) due to the $z \to -z$ symmetry of the interaction potential. The total energy change $\Delta E = \Delta E_{\rm pot} + \Delta E_{\rm int} \sim e^2[2\pi(\sigma_1 - \sigma_2)d - sd^2]$, dominated by the linear potential term for small d, is positive and the particle prefers to remain in its lattice position within phase I. In other words, phase I is always stable at small enough distances. The way in which phase I transforms to another phase at a specific distance η_c depends on the value of the asymmetry parameter A.

If A is close to its symmetric value 1, the prefactor to the linear potential energy increase $\Delta E_{\rm pot}$ is small and the transition occurs at small η_c. For $\eta > \eta_c$, the particles skip perpendicularly from plate 1 to the corresponding projected positions on plate 2. The number of hopping particles, reflected via the occupation (order) parameter x, is expected to grow continuously from 0 at η_c to a positive value for η beyond η_c.

We can determine the stability boundary of phase I by making the above simple energy argument quantitative. Let us denote by $\{\mathbf{R}_i = (X_i, Y_i)\}_{i=1}^N$ the set of lattice points for the Wigner hexagonal structure of phase I at plate 1 with lattice spacing a. Thus, taking a reference particle, say 1, from its lattice position $\mathbf{R}_1$ to the perpendicularly projected position at plate 2 implies the energy change given by

$$\frac{\Delta E(A,\eta)}{e^2} = 2\pi(\sigma_1 - \sigma_2)d + \sum_{j\neq 1}\left(\frac{1}{\sqrt{R_{1j}^2 + d^2}} - \frac{1}{R_{1j}}\right), \tag{10}$$

where $R_{1j} \equiv |\mathbf{R}_1 - \mathbf{R}_j|$. Using the summation technique of Ref. [12], we get the representation

$$\frac{\Delta E(A,\eta)}{e^2\sqrt{\sigma_1+\sigma_2}} = 2^{3/2}\pi\frac{1-A}{1+A}\eta - \frac{1}{\sqrt{2\pi}}\int_0^\infty \frac{{\rm d}t}{\sqrt{t}}\left(1 - {\rm e}^{-\eta^2 t}\right)\left[\theta_3({\rm e}^{-\sqrt{3}t})\theta_3({\rm e}^{-t/\sqrt{3}}) - 1 + \theta_2({\rm e}^{-\sqrt{3}t})\theta_2({\rm e}^{-t/\sqrt{3}})\right]. \tag{11}$$

For small η, the linear term dominates in (11) and $\Delta E > 0$. The border of stability of phase I, η_c, is identified with the balance of potential and interaction energy, $\Delta E = 0$, i.e.

$$4\pi\frac{1-A}{1+A}\eta_c = \frac{1}{\sqrt{\pi}}\int_0^\infty \frac{{\rm d}t}{\sqrt{t}}\left(1 - {\rm e}^{-\eta_c^2 t}\right)\left[\theta_3({\rm e}^{-\sqrt{3}t})\theta_3({\rm e}^{-t/\sqrt{3}}) - 1 + \theta_2({\rm e}^{-\sqrt{3}t})\theta_2({\rm e}^{-t/\sqrt{3}})\right]. \tag{12}$$

The series representation of the rhs of Eq. (12) is given in the Appendix. Since the lattice deformation is negligible in the small-η ($A \to 1$) limit, the formula (12) reduces to the exact asymptotic expression

$$\eta_c = \lambda\frac{1-A}{1+A}, \qquad \lambda = \frac{4\pi}{\frac{1}{\sqrt{\pi}}\int_0^\infty {\rm d}t\,\sqrt{t}\left[\theta_3({\rm e}^{-\sqrt{3}t})\theta_3({\rm e}^{-t/\sqrt{3}}) - 1 + \theta_2({\rm e}^{-\sqrt{3}t})\theta_2({\rm e}^{-t/\sqrt{3}})\right]}. \tag{13}$$

Using the general theory of lattice sums [14] it can be shown that

$$\frac{1}{\sqrt{\pi}}\int_0^\infty {\rm d}t\,\sqrt{t}\left[\theta_3({\rm e}^{-\sqrt{3}t})\theta_3({\rm e}^{-t/\sqrt{3}}) - 1 + \theta_2({\rm e}^{-\sqrt{3}t})\theta_2({\rm e}^{-t/\sqrt{3}})\right] = 3^{1/4}\zeta\left(\frac{3}{2}\right)\left[\zeta\left(\frac{3}{2},\frac{1}{3}\right) - \zeta\left(\frac{3}{2},\frac{2}{3}\right)\right], \tag{14}$$

where $\zeta(z,q) = \sum_{j=0}^\infty 1/(q+j)^z$ is the generalised Riemann zeta function and $\zeta(z) \equiv \zeta(z,1)$. The prefactor $\lambda \sim 0.999215\ldots$ is thus very close, but not equal, to 1.

B. Transition I $\to$ I$_x$

We next document the mechanism of a continuous phase transition at η_c from phase I to another phase coined as I$_x$ [16]. According to the results of numerical simulations, phase I$_x$ is defined in the following way: there are $N_2 = xN$ particles which are picked from the Wigner lattice α at plate 1 [with the lattice spacing a given by (9), in such a way that they form a projected hexagonal structure β on plate 2 with a lattice spacing $b > a$. An illustration for $x = 1/3$ is provided in Fig. 4a. It is seen that due to the vacancies the original hexagonal structure α is modified to the honeycomb lattice. To specify the possible values of b/a, we notice that joining arbitrary two vertices of lattice α implies a side of the hexagonal lattice β whose all points also belong to α. The primitive vectors of the hexagonal lattice α are $\mathbf{a}_1 = a(1,0)$ and $\mathbf{a}_2 = a(1/2,\sqrt{3}/2)$. Choosing the lattice vector of β as $\mathbf{b} = j\mathbf{a}_1 + k\mathbf{a}_2$ with (j,k) positive

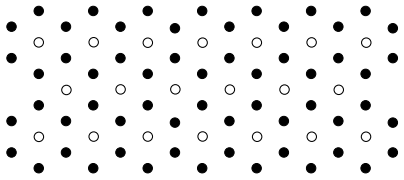

(a) Structure I_x with $x = 1/3$.

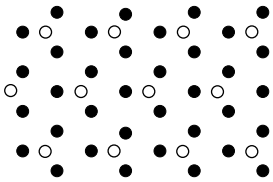

(b) Structure V_x with $x = 1/4$.

FIG. 4: Illustration. The ions on plate 1 are shown by the filled circles, those on plate 2 by empty circles.

integers such that $j+k \neq 0, 1$ [$(j,k) = (0,2)$, $(1,1)$, $(0,3)$, $(1,2)$, $(0,4)$, $(1,3)$, $(2,2)$, etc.], we have $b^2 = a^2(j^2+jk+k^2)$. Since $S/N_2 = \sqrt{3}b^2/2$, the possible values of x are constrained to

$$x \equiv \frac{N_2}{N} = \frac{a^2}{b^2} = \frac{1}{j^2+jk+k^2}, \qquad x \in \left\{\frac{1}{3}, \frac{1}{4}, \frac{1}{7}, \frac{1}{9}, \frac{1}{12}, \frac{1}{13}, \frac{1}{16}, \ldots\right\}. \tag{15}$$

The admissible discrete values of x become very dense when $x \to 0$ and we shall take x as a quasi-continuous variable in that limit. The discrete values of x considered in our analytical treatment will be just those explicitly indicated in Eq. (15). The structure I_x with $x = 1/3$ is pictured in Fig. 4a. This structure with the largest possible value of x is of special interest: particles on plate 1 form a honeycomb lattice while particles on plate 2 form a hexagonal lattice. Due to a high degree of symmetry, there are no local distortions of the two structures on plate 1 and 2; we shall coin this structure as H.

The calculation of the total energy change $E(x,\eta) - E(0,\eta)$ of phase I_x with respect to phase I is as follows:

$$\frac{E_\mathrm{I}(x,\eta) - E_\mathrm{I}(\eta)}{e^2 N_2} = 2\pi(\sigma_1-\sigma_2)d + \sum_{\substack{j\in\alpha\\ j\neq 1}}\left(\frac{1}{\sqrt{R_{1j}^2+d^2}} - \frac{1}{R_{1j}}\right) - \sum_{\substack{j\in\beta\\ j\neq 1}}\left(\frac{1}{\sqrt{R_{1j}^2+d^2}} - \frac{1}{R_{1j}}\right). \tag{16}$$

The first term on the rhs of this equation corresponds to the increase of the potential energy by taking N_2 particles from plate 1 to 2. The second term is the change in the interaction energy of a each particle transferred from plate 1 to 2, with respect to particles on α. The particles on β should not be included in that sum as the mutual interaction energy of particles on β is unchanged by their simultaneous transfer to plate 2, so the third term compensates for this. Using Ref. [12], the energy of phase I_x in terms of the function $K(\eta)$ (see the Appendix) reads

$$\frac{E_\mathrm{I}(x,\eta)}{e^2 N\sqrt{\sigma_1+\sigma_2}} = 2^{3/2}\pi\eta\left(x - \frac{A}{1+A}\right)^2 + c + \frac{x}{\sqrt{2}}\left[-K(\eta) + \sqrt{x}K(\sqrt{x}\eta)\right]. \tag{17}$$

Numerical simulation results provide strong hints that the transition from phase I with $x = 0$ to phase I_x with $x > 0$ is continuous, i.e. of second order. To have an analogy of our system of classical particles at zero temperature with a statistical model, we keep in mind that the role of the inverse temperature is played by the dimensionless distance between the plates η and the role of the free energy is played by the energy (17). The order parameter, which changes continuously from zero just at the critical point, is the plate-occupation x. For small x, the difference of the energies of phases I and I_x can be expanded in powers of x by using (17):

$$\frac{E_\mathrm{I}(x,\eta) - E_\mathrm{I}(\eta)}{e^2 N\sqrt{\sigma_1+\sigma_2}} = f(\eta)x + \frac{2^{3/2}\pi}{\lambda}\eta^2 x^{5/2} + O(x^{7/2}), \tag{18}$$

where

$$f(\eta) = 2^{3/2}\pi\frac{1-A}{1+A}\eta - \frac{1}{\sqrt{2\pi}}\int_0^\infty \frac{\mathrm{d}t}{\sqrt{t}}\left(1-\mathrm{e}^{-\eta^2 t}\right)\left[\theta_3(\mathrm{e}^{-\sqrt{3}t})\theta_3(\mathrm{e}^{-t/\sqrt{3}}) - 1 + \theta_2(\mathrm{e}^{-\sqrt{3}t})\theta_2(\mathrm{e}^{-t/\sqrt{3}})\right] \tag{19}$$

coincides with the rhs of Eq. (11) and the constant λ is defined by Eqs. (13) and (14). Note that the expansion (18) of the energy in the order parameter x is not analytic due to the long-range Coulomb interaction. This contradicts the standard Ginsburg-Landau (GL) theory of phase transitions in which the thermodynamic potential (the energy in our case), assumed to be a smooth function of the order parameter, is expanded in powers of the order parameter, taking due account of the symmetry of the system. Our energy change (18) has no symmetry invariance with respect to a transformation of x. This contrasts with the transitions between structures II, III and IV (see section V below)

which turn out to belong to the GL family. In addition to involving non-integer powers of the order parameter, note also that our expansion (18) starts at order 1 which is in contrast with the GL expansion starting with the x^2 term (in the absence of an external field).

The free variable x has to be chosen in such a way that it provides the minimal value of the energy. The extremum condition for $E_{\rm I}(x,\eta)$, $\partial_x E_{\rm I}(x,\eta)=0$, when applied to (18) takes the form

$$0 = f(\eta) + \frac{5\sqrt{2}\pi}{\lambda}\eta^2 x^{3/2} + O(x^{5/2}). \tag{20}$$

The critical point η_c, identified with the condition $f(\eta_c)=0$, is equivalent to the previously derived stability border (12) for phase I. The function $f(\eta)$ in (19) is dominated by the linear term for small η, so that $f(\eta)>0$ for $\eta<\eta_c$, while $f(\eta)<0$ for $\eta>\eta_c$, and we can write in the neighbourhood of the critical point η_c that $f(\eta)\sim g(\eta_c-\eta)$ with a positive prefactor $g>0$. It is then readily concluded that $x=0$ for $\eta<\eta_c$ while $x\propto(\eta-\eta_c)^{2/3}$ for $\eta>\eta_c$.

We recall that the above analytic treatment is rigorous only in the asymptotic limit ($A\to 1, \eta_c\to 0$) where one can de dispensed with considering lattice distortions; for other asymmetry parameters A, the values of critical indices should be checked numerically along the whole critical line between phases I and I_x.

III. "SMALL" VALUES OF A, TRANSITION BETWEEN PHASES I AND V_x

If the asymmetry parameter A is close to zero ("small A"), the prefactor in $\Delta E_{\rm pot}$ is large and the transition from phase I to another phase occurs at large η_c. A particle hopping from plate 1 to plate 2 can "lose" the information about its lattice Wigner position in phase I and can create, together with all other hopping particles, a completely new energetically favourable structure. Since local deformations of the lattices α and β are substantial for large η_c, the order of the phase transition should be determined numerically.

Phase V_x is the counterpart of phase V, which is the phase providing the lowest energy for symmetrically charged plates at sufficiently large distances η. It consists of two hexagonal structures, lattice α (spacing a) at plate 1 with $N_1=(1-x)N$ particles and lattice β (spacing b) at plate 2 with $N_2=xN$ particles, with some shift. The lattice spacings are given by

$$\frac{S}{N} = \frac{\sqrt{3}}{2}a^2(1-x) = \frac{\sqrt{3}}{2}b^2 x, \tag{21}$$

where x can be considered a continuous variable. When calculating the interaction energy between particles on α and those on β, it is advantageous to evaluate the *full* interaction energy of one β-particle with all α-particles and then simply multiply the result by N_2. Using the summation techniques developed in Ref. [12] we obtain the energy of phase V_x in the form

$$\frac{E_{\rm V}(x,\eta)}{Ne^2\sqrt{\sigma_1+\sigma_2}} = 2^{3/2}\pi\eta\left(x-\frac{A}{1+A}\right)^2 + c\left[(1-x)^{3/2}+x^{3/2}\right] + J(x,\eta), \tag{22}$$

where c is the known Madelung constant [12] and

$$J(x,\eta) = x\sqrt{1-x}\,\frac{1}{2^{3/2}\sqrt{\pi}}\int_0^\infty \frac{\mathrm{d}t}{\sqrt{t}}\left[-\mathrm{e}^{-t\eta^2(1-x)}+\sqrt{3}\mathrm{e}^{-3t\eta^2(1-x)}\right] \times\left\{\left[\theta_3(\mathrm{e}^{-\sqrt{3}t})\theta_3(\mathrm{e}^{-t/\sqrt{3}})-1-\frac{\pi}{t}\right]+\left[\theta_2(\mathrm{e}^{-\sqrt{3}t})\theta_2(\mathrm{e}^{-t/\sqrt{3}})-\frac{\pi}{t}\right]\right\}. \tag{23}$$

The first term on the rhs of (22) is the excess energy due to the non-neutrality of each of the plates, the second term corresponds to the neutralised intra-layer sums within plate 1 and within plate 2 and the integral $J(x,\eta)$ describes the inter-layer interaction between electro-neutral plates 1 and 2.

Analytically, the transition from phase I to V_x is discontinuous (of first order), accompanied by a small skip of x from zero to a non-zero value. It turns out that neglecting local lattice distortions is an inadequate simplification of the problem: our numerical results show that the transitions between phases I and V_x are continuous.

IV. LARGE DISTANCE ASYMPTOTICS

Numerical approaches face serious accuracy problems when dealing with two plates at large distances because the interaction energy of the plates is small. On the other hand, our analytic treatment of large-distance characteristics of

phase V_x is asymptotically exact. The key point is that irrespective of the particular geometry of the two structures on plates 1 and 2, the inter-layer term J in Eq. (22) pertains to *electro-neutral* plates, and decays exponentially with distance η. In the large-η limit, we can neglect this contribution and consider only intra-layer interactions (from which algebraic decay ensues as becomes clear below):

$$\frac{E_{\mathrm{V}}(x,\eta)}{Ne^2\sqrt{\sigma_1+\sigma_2}} \underset{\eta\to\infty}{\sim} 2^{3/2}\pi\eta\left(x-\frac{A}{1+A}\right)^2 + c\left[(1-x)^{3/2}+x^{3/2}\right]. \tag{24}$$

One recognises the same structure as invoked in Ref. [17]. The energy minimisation condition

$$\frac{\partial E_{\mathrm{V}}(x,\eta)}{\partial x} = 0 = 2^{5/2}\pi\eta\left(x-\frac{A}{1+A}\right) + \frac{3}{2}c\left(\sqrt{x}-\sqrt{1-x}\right) \tag{25}$$

implies the asymptotic $\eta\to\infty$ behaviour

$$x \underset{\eta\to\infty}{\sim} x_{\mathrm{neutr}} - \frac{3(-c)}{2^{7/2}\pi}\frac{1-\sqrt{A}}{\sqrt{1+A}}\frac{1}{\eta} \tag{26}$$

Since the Madelung constant c is a negative number, x goes to its asymptotic "neutral" value $x_{neutr} = A/(1+A)$ from below. As soon as $A \neq 1$, the plates (each as a whole) remain charged up to infinite distance. The energy behaves as

$$\frac{E_{\mathrm{V}}(\eta)}{Ne^2\sqrt{\sigma_1+\sigma_2}} \underset{\eta\to\infty}{\sim} c\left[\left(\frac{1}{1+A}\right)^{3/2}+\left(\frac{A}{1+A}\right)^{3/2}\right] - \frac{9c^2}{2^{11/2}\pi}\frac{(1-\sqrt{A})^2}{1+A}\frac{1}{\eta}. \tag{27}$$

We conclude that at large distances also, the ground-state energy approaches its asymptotic value from below, with a $-1/\eta$ correction. This implies that the force (or more precisely the pressure) felt by the plates is attractive, and behaves as $-1/\eta^2$. This is in stark contrast to the symmetric situation $A = 1$, where the force decays much faster (exponentially). It is worth emphasizing here that for all parameter values, the force on one plate is attractive.

V. PHASES II, II$_x$, III AND IV

In the vicinity of the line $A = 1$, there is a sequence of phases II, III and IV which are dominant for small and intermediate distances between the plates. They have an order parameter $x = 1/2$. "Soft" phase II [18] corresponds to a rectangular lattice with an aspect ratio $\Delta = |\boldsymbol{a}_2|/|\boldsymbol{a}_1|$ varying in the interval $(1, \sqrt{3})$, see Fig. 5a for the definition of lattice vectors $\mathbf{a}_1$ and $\mathbf{a}_2$. The "rigid" structure III with $\Delta = 1$ corresponds to the couple of square lattices, one for each plate, shifted relative to each other by a half-period. Soft phase IV consists of two staggered rhombic lattices with a varying angle φ between the primitive translation vectors. Each of these phases also corresponds to the ground state of asymmetrically charged plates, in a certain region of the parameters A (close to 1) and η. According to numerical simulations, there do not exist generalisations of phases III and IV with the particle occupation x different from 1/2.

It can be shown that the analysis performed in the symmetric case $A = 1$ extends to the present transitions, from which one can conclude to the mean-field nature of critical indices (Ising-like, with for instance an exponent $\beta = 1/2$ instead of $\beta = 2/3$, as reported for the $\mathrm{I}\to\mathrm{I}_x$ and $\mathrm{I}\to\mathrm{V}_x$ transitions). It is noteworthy that for one model with the fixed asymmetry parameter A, by changing the plate distance η, we get a sequence of phase transitions with different critical indices.

Only special generalisations of phase II were observed in numerical simulations. In structure II, the whole columns of black and white particles are distributed successively between plates 1 and 2, respectively. We can formally assign to this periodic repetition the symbol [bw]. Another observed sequence [bbw] corresponds to phase II_x with $x = 1/3$. All other II_x structures can be constructed by using these two building elements [bw] and [bbw]. Phase II_x with $x = 2/5$, pictured in Fig. 5a, is represented formally from top to bottom as a periodically repeated sequence [bw][bbw]. Another considered phase II_x with $x = 3/7$ corresponds to the sequence [bw][bw][bbw]. The last phase II_x considered in the analytical treatment corresponds to the sequence [bw][bbw][bbw] and is characterised by $x = 3/8$. The series representations of the energies of the II_x structures can be derived along similar lines as for phase II.

VI. SNUB 1 PHASE

Archimedean tiling by regular polygons requires that the arrangement of tiles around each vertex be the same. In numerical simulations of the asymmetrically charged plates, we observed the so-called "snub square tiling" presented

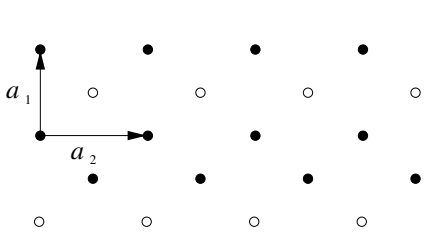

(a) Structure II_x with $x = 2/5$.

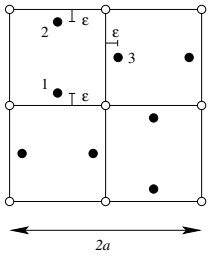

(b) Snub 1 phase with $x = 1/3$.

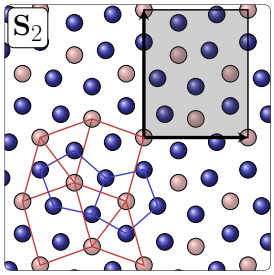

(c) Snub 2 phase found in EA with $x = 1/3$.

FIG. 5: Illustration of structures: II_x, Snub 1 (S_1) and Snub 2 (S_2).

in Fig. 5b: this rigid structure arises e.g. by projecting white particles on plate 2, which form a square lattice of side a, to plate 1 occupied by black particles. The unit $(2a) \times (2a)$ cell contains 8 black and 4 white particles, so that $x = 4/(4+8) = 1/3$ for this structure. The value of ε is fixed by the condition that the distance between particles 1 and 2 is equal to that between particles 1 and 3, the square-lattice spacing a follows from the electro-neutrality condition:

$$\varepsilon = a\left(1 - \frac{\sqrt{3}}{2}\right), \qquad a = \sqrt{\frac{3}{\sigma_1 + \sigma_2}} = \sqrt{\frac{3}{n_1 + n_2}}. \tag{28}$$

The positions of particles on plate 2 can be enumerated simply as $a(j,k)$, where j,k are integers. The positions of particles on plate 1 can be generated from 8 basic positions in an elementary $(2a) \times (2a)$ cell, $(a/2, \varepsilon)$, $(a/2, a-\varepsilon)$, $(a+\varepsilon, a/2)$, $(2a-\varepsilon, a/2)$, $(\varepsilon, -a/2)$, $(a-\varepsilon, -a/2)$, $(3a/2, -\varepsilon)$, $(3a/2, -a+\varepsilon)$, by adding all possible shifts $2a(j,k)$ with j,k-integers. The total energy of the snub 1 phase can be readily expressed as series of the generalised Misra functions (formulas not shown).

Appendix: Series representations of lattice sums

The rhs of Eq. (12) can be transformed into $K(\eta_c) + 4\pi\eta_c$, where the function K depends on distance η as

$$K(\eta) = \frac{1}{\sqrt{\pi}} \int_0^\infty \frac{\mathrm{d}t}{\sqrt{t}} \left(1 - \mathrm{e}^{-\eta^2 t}\right) \left\{ \left[\theta_3(\mathrm{e}^{-\sqrt{3}t})\theta_3(\mathrm{e}^{-t/\sqrt{3}}) - 1 - \frac{\pi}{t}\right] + \left[\theta_2(\mathrm{e}^{-\sqrt{3}t})\theta_2(\mathrm{e}^{-t/\sqrt{3}}) - \frac{\pi}{t}\right] \right\}. \tag{A.1}$$

In terms of the functions

$$\begin{aligned} I_2(x,y) &\equiv \int_0^\pi \frac{dt}{\sqrt{t}} \mathrm{e}^{-xt/\pi^2} \mathrm{e}^{-y\pi^2/t} \left[\theta_2(\mathrm{e}^{-\sqrt{3}t})\theta_2(\mathrm{e}^{-t/\sqrt{3}}) - \frac{\pi}{t}\right] \\ &= 2\sum_{j=1}^\infty (-1)^j \left[z_{3/2}(x, y + j^2/\sqrt{3}) + z_{3/2}(x, y + j^2\sqrt{3})\right] + 4\sum_{j,k=1}^\infty (-1)^j (-1)^k z_{3/2}(x, y + j^2/\sqrt{3} + k^2\sqrt{3}), \end{aligned}$$

$$\begin{aligned} I_3(x,y) &\equiv \int_0^\pi \frac{dt}{\sqrt{t}} \mathrm{e}^{-xt/\pi^2} \mathrm{e}^{-y\pi^2/t} \left[\theta_3(\mathrm{e}^{-\sqrt{3}t})\theta_3(\mathrm{e}^{-t/\sqrt{3}}) - 1 - \frac{\pi}{t}\right] \\ &= 2\sum_{j=1}^\infty \left[z_{3/2}(x, y + j^2/\sqrt{3}) + z_{3/2}(x, y + j^2\sqrt{3})\right] + 4\sum_{j,k=1}^\infty z_{3/2}(x, y + j^2/\sqrt{3} + k^2\sqrt{3}) - \pi z_{1/2}(x,y), \end{aligned}$$

$$I_4(x,y) \equiv \int_0^\pi \frac{dt}{\sqrt{t}} \mathrm{e}^{-xt/\pi^2} \mathrm{e}^{-y\pi^2/t} \left[\theta_4(\mathrm{e}^{-\sqrt{3}t})\theta_4(e^{-t/\sqrt{3}}) - 1\right] = 4\sum_{j,k=1}^\infty z_{3/2}(x, y + (j-\frac{1}{2})^2/\sqrt{3} + (k-\frac{1}{2})^2\sqrt{3}) - \pi z_{1/2}(x,y)$$

$K(\eta)$ can be expressed as

$$K(\eta) = \frac{1}{\sqrt{\pi}}[2I_3(0,0) - I_3((\pi\eta)^2, 0) - I_3(0, \eta^2) + I_2(0,0) - I_2((\pi\eta)^2, 0) + I_4(0,0) - I_4(0, \eta^2)], \tag{A.2}$$

where we have introduced the generalised Misra z functions as $z_\nu(x,y) = \int_0^{1/\pi} \frac{\mathrm{d}t}{t^\nu} \mathrm{e}^{-xt}\mathrm{e}^{-y/t}$, $y > 0$. The above series expansions for I_2, I_3, I_4 enjoy exceptional convergence properties in j and k. This allows for a fast and precise calculation of these quantities, and thus of K (or likewise, the Madelung constant c). In numerical calculations using a symbolic language, the series over the generalised Misra functions are truncated after the 5th terms (i.e. $j = k = 5$); for c, this yields an accuracy of 17 decimal digits.

---

[1] M. Mazars, Phys. Rep. **500**, 43 (2011).
[2] P.J. Steinhardt, D.R. Nelson and M. Ronchetti, Phys. Rev. B **28**, 784 (1983).
[3] M. Mazars, EPL, **84**, 55002 (2008).
[4] A. Okabe, B. Boots, K. Sugihara and S. Nok Chiu, *Spatial Tessellations: Concepts and Applications of Voronoi Diagrams (Second Edition)*. (John Wiley & Sons, Inc. - New York - 2000).
[5] W. Mickel, S. C. Kapfer, G. E. Schröder-Turk and K. Mecke, J. Chem. Phys. **138**, 044501 (2013).
[6] D. Gottwald, G. Kahl, and C. Likos, J. Chem. Phys. **122**, 204503, (2005)
[7] R. Byrd, P. Lu, J. Nocedal, and C. Zhu, SIAM J. Scient. Stat. Comput. **16**, 1190, (1995).
[8] J.-J. Weis, D. Levesque and S. Jorge, Phys. Rev. B **63**, 045308 (2001).
[9] B. Grünbaum and G.C. Shepard *Tilings and patterns* (W.H. Freeman and Company - New York - 1987).
[10] M. Mazars, EPL, **110**, 26003 (2015).
[11] While the energy only depends on η, $A = \sigma_2/\sigma_1$ and $x = n_2/(n_1 + n_2)$ [see e.g. Eq. (8)], it is convenient, for the sake of presentation, to rewrite its arguments explicitly as the set $(\eta, \sigma_1, n_1, \sigma_2, n_2)$. It is also worthwhile here emphasizing that in practice, only η and A are fixed, x being selected by the energy minimum requirement.
[12] L. Šamaj and E. Trizac, Phys. Rev. B **85**, 205131 (2012).
[13] R. D. Misra, Math. Proc. Cambridge Philos. Soc. **36**, 173 (1940); M. Born and R. D. Misra, Math. Proc. Cambridge Philos. Soc. **36**, 466 (1940).
[14] I. J. Zucker, J. Math. Phys. **15**, 187 (1974); I. J. Zucker and M. M. Robertson, J. Phys. A **8**, 874 (1975).
[15] S.-K. Ma, Modern Theory of Critical Phenomena (Westview Press, New York, 1976).
[16] All structures indexed by x, such as I_x, II_x, V_x and DV_x, correspond to a family of arrangements having a common pattern, with characteristic length scales depending on x.
[17] R. Messina, C. Holm, and K. Kremer, Phys. Rev. E **64**, 021405 (2001).
[18] "Soft" as opposed to "rigid" refers here to the fact that the structure geometry depends on distance η.